Supplementary Information

A Handheld Tool for Temporal and Spatial Young's Modulus Characterization of Soft Materials: Towards Point-of-Care Soft Tissue Assessment

Saitarun Nadipineni, Mohamed Adhnan Thaha, Kaspar Althoefer and Thilina Dulantha Lalitharatne*

Table of Contents for Supplementary Information

Other supporting information for this manuscript include the following;

Supplementary Video 1.

Supplementary Notes

Note 1. Hertz contact model

When tissue is indented, the Effective Young's Modulus (E^*), which consists of the Young's modulus of the indenter (E_i) and the tissue (E_t) can be described as,

$$\frac{1}{E^*} = \frac{1 - v_i^2}{E_i} + \frac{1 - v_t^2}{E_t} \tag{1}$$

where v_i and v_t are Poisson's ratio of the indenter and tissue [1,2]. In the case of spherical indentation where the indenter is significantly rigid than the tissue, $E_i \gg E_t$, E^* can be given as,

$$E^* = \frac{E_t}{1 - {v_t}^2} \tag{2}$$

The relation between E^* and the contact radius of the deformation (a) is given as,

$$E^* = \frac{3}{4}\frac{F_{R-t}\, r_i}{a^3} \tag{3}$$

where F_{R-t} is the reaction force of the tissue and r_i is the radius of the of the indenter. Furthermore,

$$a = \sqrt{r_i\, h_t} \tag{4}$$

where h_t is the deformation of the tissue. By combining equations 2, 3 and 4 the Young's modulus of the tissue is given as,

$$E_t = \frac{3}{4}\, F_{R-t}\, (1 - v_t^2)\, {r_i}^{-\frac{1}{2}}\, {h_t}^{-\frac{3}{2}}. \tag{5}$$

Note 2. Magnetometer calibration

The magnetometer data showed saturation if the magnet was too close. To determine the saturation distance, the *findpeaks* function in Matlab was used to identify the local maxima. A minimum prominence of 7700 μT was used. The mean distance of the detected peaks is ~1 mm. Hence, the magnetometer saturates if the magnet is closer than 1 mm. Beyond this point, the magnetic field resembles the trend in existing [3]. Therefore, data beyond 1 mm was used for calibration. The power regression model was used for calibration,

$$d'_m = \alpha B^{\beta} + \gamma \quad (6)$$

where d'_m is the predicted distance of the magnet, B is the magnetic field. The coefficients of the model are $\alpha = 224.98$, $\beta = -0.43$ and $\gamma = -3.47$. The power model yielded the best approximation of the magnet's distance (d_m) with $R^2 = 0.9995$ (Supplementary Fig. 1b).

To evaluate the performance of the model, the calibration procedure was repeated 10 times. Equation 6 was used to compare d'_m with d_m (Supplementary Fig. 1c). This resulted in a Mean Absolute Error (MAE) of 0.20 mm, and a Root Mean Square Error (RMSE) of 0.28 mm. This shows the calibration model is robust for estimating the distance of the magnet.

Note 3. Use of camera calibration

Before the real-world positions of the ArUco markers are detected, the camera images must be undistorted [4]. The distortion coefficients obtained from calibration can be used for this,

$$Distortion\ Coefficents = [k_1 \quad k_2 \quad p_1 \quad p_2 \quad k_3] \quad (7)$$

where $k_1 = 0.08$, $k_2 = -0.78$, $k_3 = 1.06$ are the radial coefficients and $p_1 = 0.0002$ and $p_2 = -0.0050$ are the tangential coefficients.

Radial distortion occurs when light rays that pass through the camera lens are not refracted evenly. The two types of radian distortion are barrel and pincushion distortion. Barrel distortion can be noticed when the outer edges of the image are bulged outward and pincushion distortion can be noticed when the outer edges curve inward [5]. Given a normalized point **P** whose distorted coordinates are $[x_{distorted}, y_{distorted}]^T$, radial distortions can be modelled as,

$$r^2_{distorted} = x^2_{distorted} + y^2_{distorted}\ , \quad (8)$$

$$x_{radial}^{distorted} = x_{undistorted}(1 + k_1\, r_{distorted}^2 + k_2\, r_{distorted}^4 + k_3\, r_{distorted}^6)\,, \quad (9)$$
$$y_{radial}^{distorted} = y_{undistorted}(1 + k_1\, r_{distorted}^2 + k_2\, r_{distorted}^4 + k_3\, r_{distorted}^6)\,,$$

where $r_{distorted}$ is the distance between point **P** and the origin of the coordinate system and $[x_{undistorted}, y_{undistorted}]^T$ are undistorted points. In the case of tangential distortion,

$$x_{tangental}^{distorted} = x_{undistorted} + 2\, p_1\, x_{undistorted}\, x_{undistorted} \quad (10)$$
$$+\ p_2\,(r_{distorted}^2 + 2\, x_{undistorted}^2)\,,$$
$$y_{tangental}^{distorted} = y_{undistorted} +\ p_1\,(r_{distorted}^2 + 2\ y_{undistorted}^2)$$
$$+ 2\, p_2\, x_{undistorted}\, x_{undistorted}.$$

By combining equations 9 and 10, a joint model with both distortions is define as,

$$x_{distorted} = x_{radial}^{distorted} + x_{tangental}^{distorted}\,, \quad (11)$$
$$y_{distorted} = y_{radial}^{distorted} + y_{tangental}^{distorted}\ .$$

The undistorted image can be used to estimate the real-world position of the ArUco marker. For this, the camera intrinsics matrix (K) is necessary,

$$K = \begin{bmatrix} f_x & 0 & c_x \\ 0 & f_y & c_y \\ 0 & 0 & 1 \end{bmatrix} \quad (12)$$

where $f_x = 1469.52$ and $f_y = 1480.77$ are the focal lengths and $c_x = 948.01$ and $c_y = 573.66$ are the optical centers. The world-coordinates can be found using K, and the pixel coordinates (u, v),

$$T = \begin{bmatrix} R & t \\ 0 & 1 \end{bmatrix}, \quad (13)$$

$$s\begin{pmatrix} u \\ v \\ 1 \end{pmatrix} = K\ T\begin{pmatrix} X \\ Y \\ Z \\ 1 \end{pmatrix}, \quad (14)$$

where T is the homogenous transformation matrix consisting of the rotation matrix R and the translation vector $t = [t_x \quad t_y \quad t_z]^T$. The skew coefficient is s and the projected world coordinates of (u, v) are expressed as X, Y, Z. Given the camera's coordinate system remains constant, t informs the translation of the ArUco marker.

Note 4. Position estimation

To estimate the relative position of SensoPal from the phantom's origin, the Rodregus rotation formula was used. The translation and rotation vectors of origin (ID 1) and target (ID 0) ArUco markers are defined as t_{origin} , t_{target} , r_{origin} and r_{target}. The t_{origin} is adjusted by using offset values, this to move the origin marker's position to the phantom's origin,

$$t_{origin} = \begin{bmatrix} t_x^{origin} - x_{offset}^{origin} & t_y^{origin} - y_{offset}^{origin} & t_z^{origin} - z_{offset}^{origin} \end{bmatrix}^T, \quad (15)$$

where $x_{offset}^{origin} = 60$ mm, $y_{offset}^{origin} = 17$ mm and $z_{offset}^{origin} = 2$ mm are the respective offsets. The rotation matrix R is found using the Rodregus rotation formula [6,7],

$$u = \begin{pmatrix} u_x \\ u_y \\ u_z \end{pmatrix}, \quad (16)$$

$$R(u,\theta) = I\cos\theta + uu^T(1-\cos\theta) + \hat{u}\sin\theta\,, \quad (17)$$

where u is a unit vector along x, y and z axis respectively. The rotation angle along the respective axis is expressed as θ, I is an identity matrix and $\hat{u}$ is the cross-product matrix. Equation 17 can be used to find the rotation matrix using the origin (R_{origin}). The relative translation ($t_{relative}$) of the target ArUco marker can be found in the following way,

$$t_{relative} = R_{origin}^T\left(t_{target} - t_{origin}\right). \quad (18)$$

Note 5. Sample selection

The external composition of the human body is complex due to various underlying tissues which result in different Young's modulus values depending on the region of the body. Hence, for our experiments we mainly selected silicone samples which fall in the Young's modulus range of skeletal muscle (50 – 170 kPa) and skin (60 – 850 kPa) [8]. This provides a good range for selecting commercially available silicone rubbers which can simulate tissue samples. For the human experiments conducted in this work, six silicone samples are suitable as they mitigate and limit cognitive biases in the experimental results. The Young's modulus values obtained from human experiments are dependent on the various indentation speeds. Due to this reason, we performed a quasi-static experiment with silicone samples to obtain Young's modulus value which does not have a high dependence on indentation speed. This provided a good basis for understanding whether the selected samples were suitable. Since the height of our samples are ~30 mm, we used 0.3 mm/s (strain rate of 0.1/s) as our quasi-static indentation speed [9]. These results showed that the "softest sample" (Ecoflex Gel 2) had a Young's modulus of ~30 kPa and the "stiffest sample" had a Young's modulus of ~280 kPa.

Based on these results, the fabricated silicone samples were used for the experiments. The Young's modulus values measured at this speed are close to existing literature [10]. After the human experiments were completed, high speed indentation tests were performed with the median indentation speed (19 mm/s). As expected, the high-speed indentations yielded higher Young's modulus values across all samples. The results of the quasi-static indentation and comparison between the two indentation speeds are shown in Supplementary Fig. 3.

Note 6. Weighted centroid analysis

This note explains how weighted centroids of the final palpation points were found. These palpation points had a Euclidean distance below 15 mm ($l \leq 15$ mm). This will provide an understanding of how far the localizations of the participants were. The weighted centroids of these palpation points can help determine the weighted average positions. The weight of each ith palpation point is based on the Young's modulus. This will ensure the points with higher Young's modulus get more importance when taking the average, which will keep the average closer to the nodules' centers.

$$(x_c\ , y_c) = \left(\frac{\sum_{i=1}^{N} x_i\, E_{ti}}{\sum_{i=1}^{N} E_{ti}}\ , \frac{\sum_{i=1}^{N} y_i\, E_{ti}}{\sum_{i=1}^{N} E_{ti}} \right) \tag{19}$$

where $(x_c\ , y_c)$ is the position of the weighted centroid found from N palpations. Using equation 19, the weighted centroid of the final palpation points of the respective nodule were found (Supplementary Fig. 10a). The Euclidean distance between the weighted centroids and nodule centers is presented in Supplementary Fig. 10b. It can be observed that the Euclidean distances between the weighted centroid and the nodule centers are very similar. This indicates that participants who were able to identify the nodules effectively were close to the nodule centers (< 10 mm).

Supplementary Figures

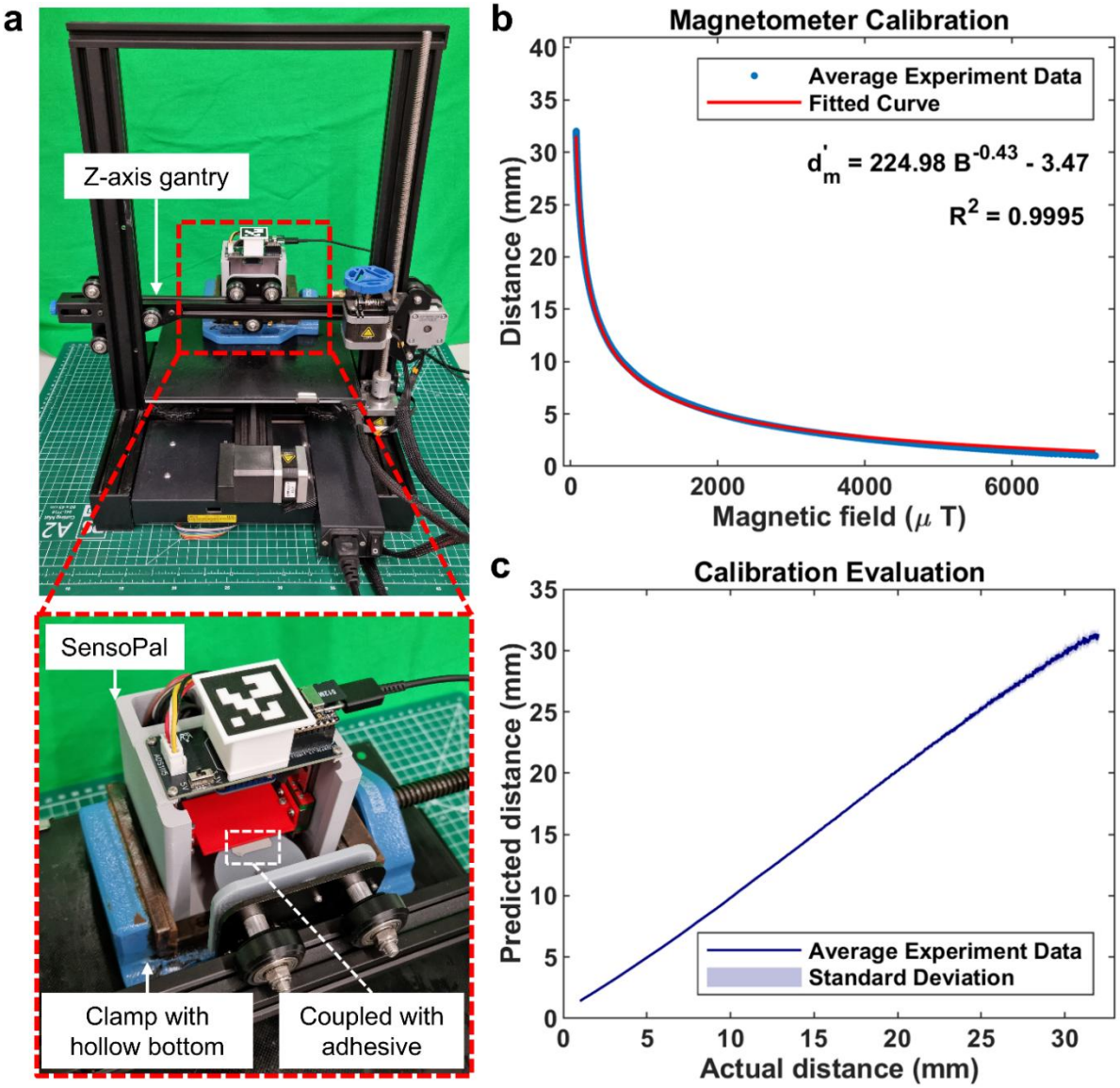

Supplementary Fig. 1 a) The hardware set up for calibrating the magnetometer of SensoPal is shown here. SensoPal was held in place by using a heavy clamp with a hollow bottom. The gantry of the modified 3D printer and the palpation platform of SensoPal were coupled using double sided tape. The gantry moved along the z-axis, and the magnetometer data was acquired. b) The average experiment data of 10 trials is shown using blue dots. The coefficients of the fitted power model and R^2 value are also shown here. This model allows us to predict the distance of the magnet from the magnetometer using its magnetic field measurements. The standard deviation in the magnetic field across all trials was negligible. c) The calibration model was evaluated by repeating the calibration procedure 10 times. The average relation between the actual and predicted distances is shown here. The shaded area represents standard deviation.

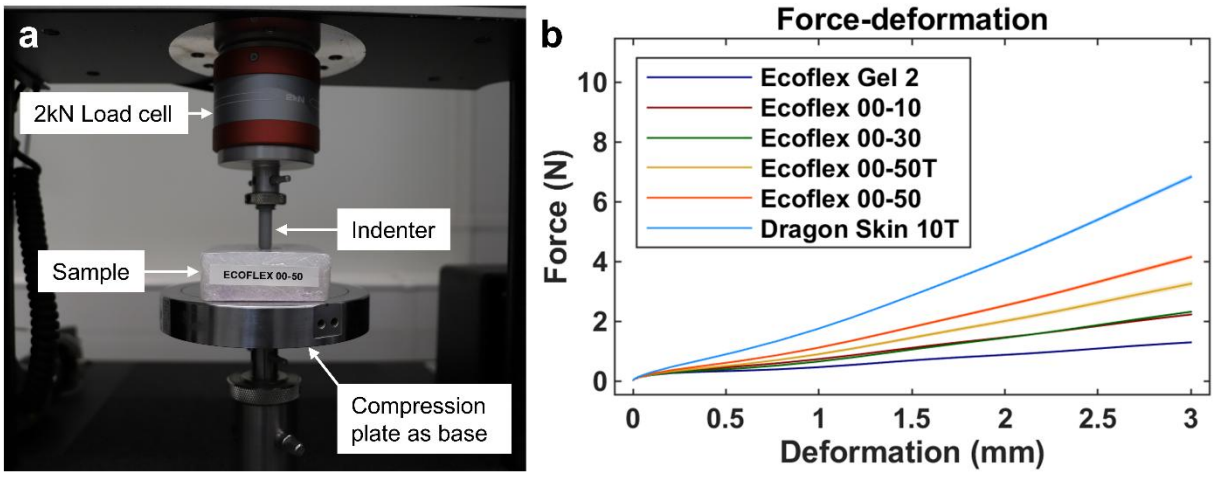

Supplementary Fig. 2 An Instron 68-TM commercial materials testing machine was used as a ground truth to compare with SensoPal's measurements. a) The testing setup for one sample is shown here. A compression plate was used as a base to place the silicone samples. A custom 3D printed intender was attached to the 2kN load cell using a slip ring. b) The average force-deformation curves for 6 trials per sample are shown here. The shaded area represents the standard deviation. The "T" character in Ecoflex 00-50T and Dragon Skin 10T indicates the addition of silicone thinner.

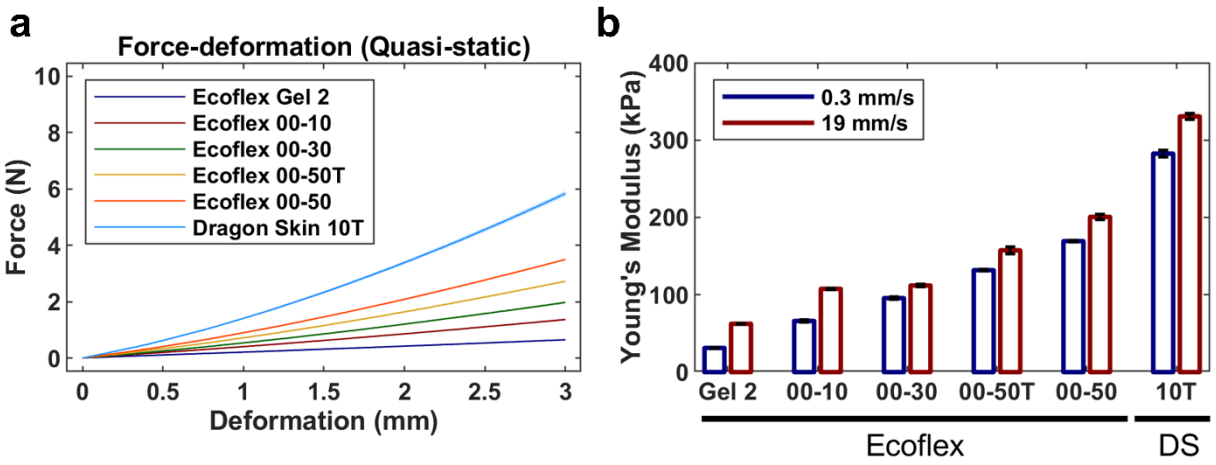

Supplementary Fig. 3 a) The average quasi-static force-deformation curves for 6 trials are shown here. The shaded area represents the standard deviation. b) The average Young's modulus values for the quasi-static (0.3 mm/s) and high-speed indentation (19 mm/s) are shown here. The black bars represent the standard deviations. The "T" character in Ecoflex 00-50T and Dragon Skin 10T indicates the addition of silicone thinner.

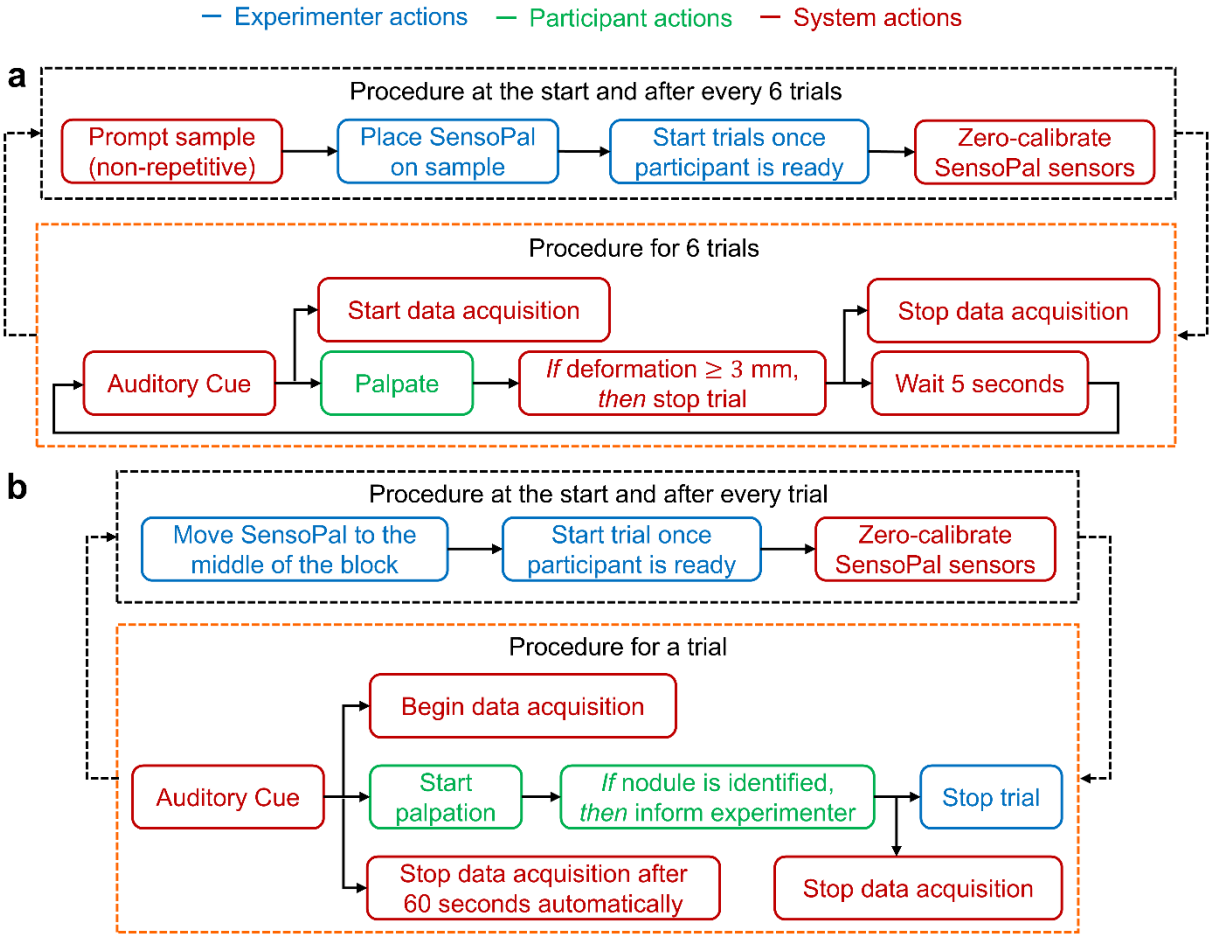

Supplementary Fig. 4 The flow diagrams show the main steps followed during human experiments. The boxes and text highlighted in blue represent experimenter actions, green represents the participant's actions and red represents the hardware system's actions (computer, SensoPal and camera). a) The experiment protocol for "Young's modulus measurement performance" is shown here. b) The experiment protocol for "Stiffness map generation with proposed system" is shown here.

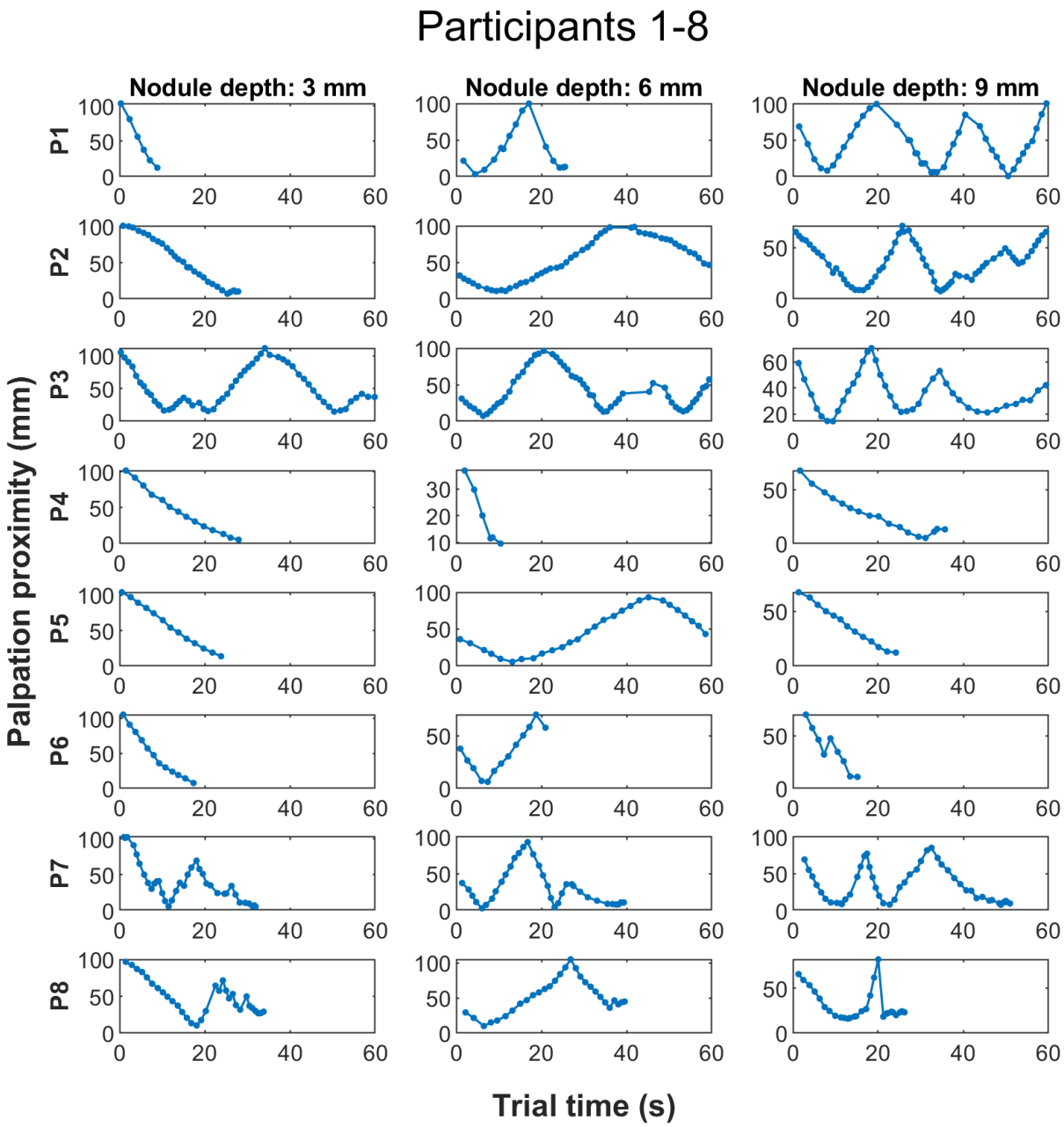

Supplementary Fig. 5 Palpation proximity with trial time for participants 1-8. The rows represent the trial data of each participant (1-8) and columns correspond to the nodule depth. The participant number is indicated with the "P" notation.

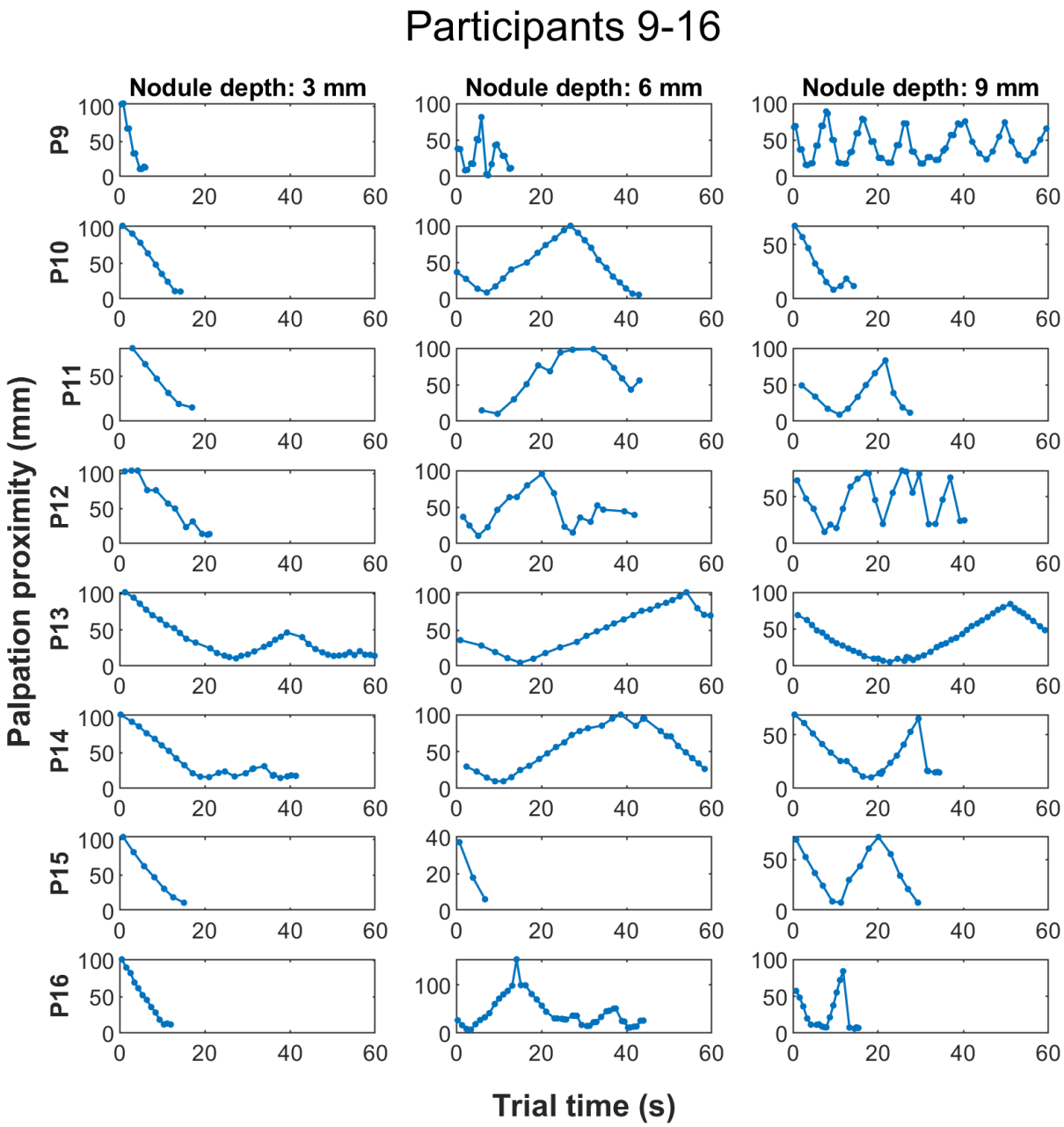

Supplementary Fig. 6 Palpation proximity with trial time for participants 9-16. The rows represent the trial data of each participant (9-16) and columns correspond to the nodule depth. The participant number is indicated with the "P" notation.

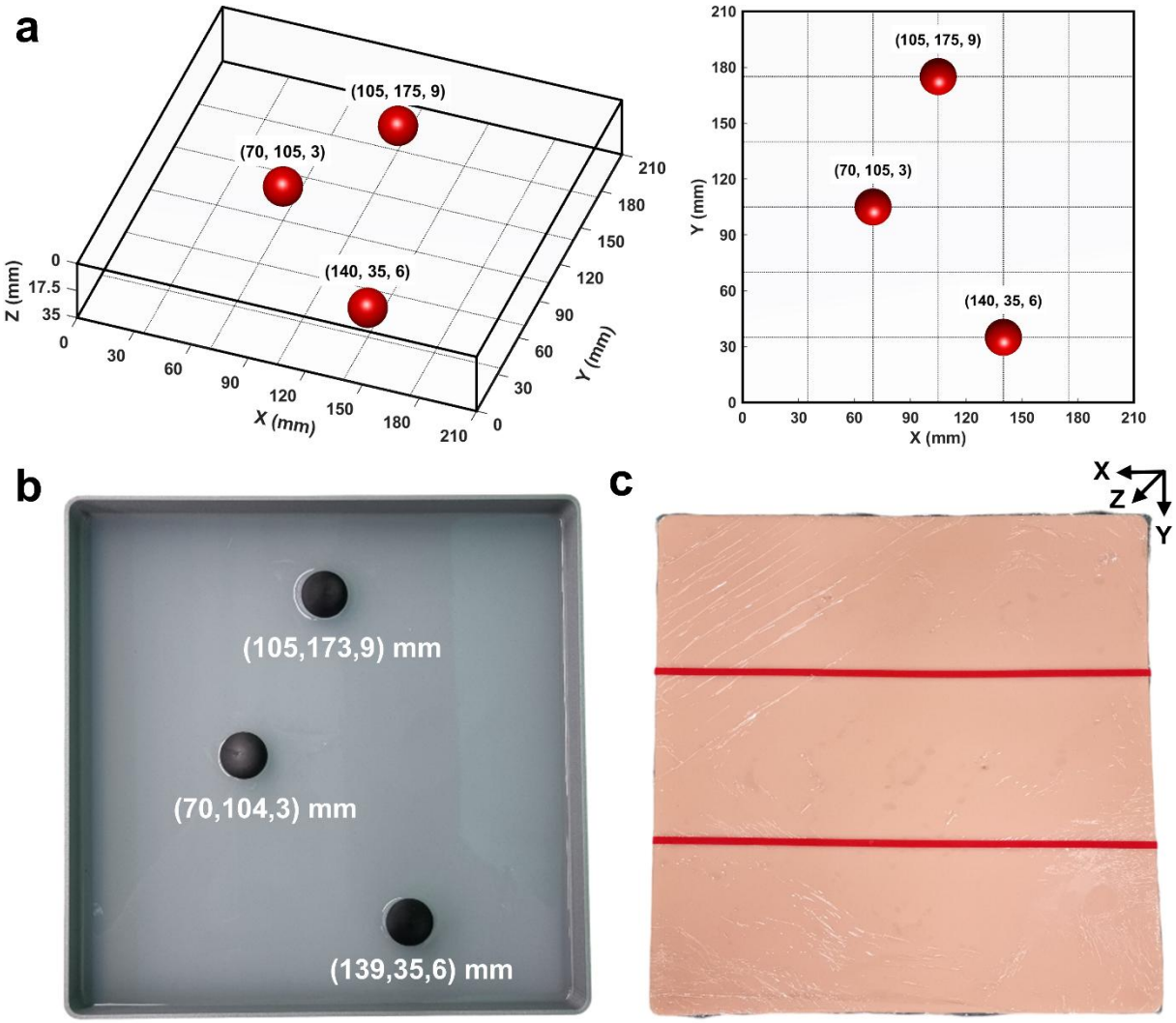

Supplementary Fig. 7 a) A 3D view of the theoretical phantom is shown on the left with the expected nodule positions in the text above each nodule. The bird's eye view of the phantom is on the right. The grid lines present the divisions used (5 divisions) to space the nodules according to the phantom's dimensions. b) The measured positions of each nodule when they were securely held by silicone layers is shown here. The positions shown are averages of five measurements. The measurements indicate the true positions of the nodules are identical to the theoretical positions. To ensure the position of each nodule accurately, a mold was used to create inverses of each nodule. c) The position of the origin which was maintained during the experiments is shown here.

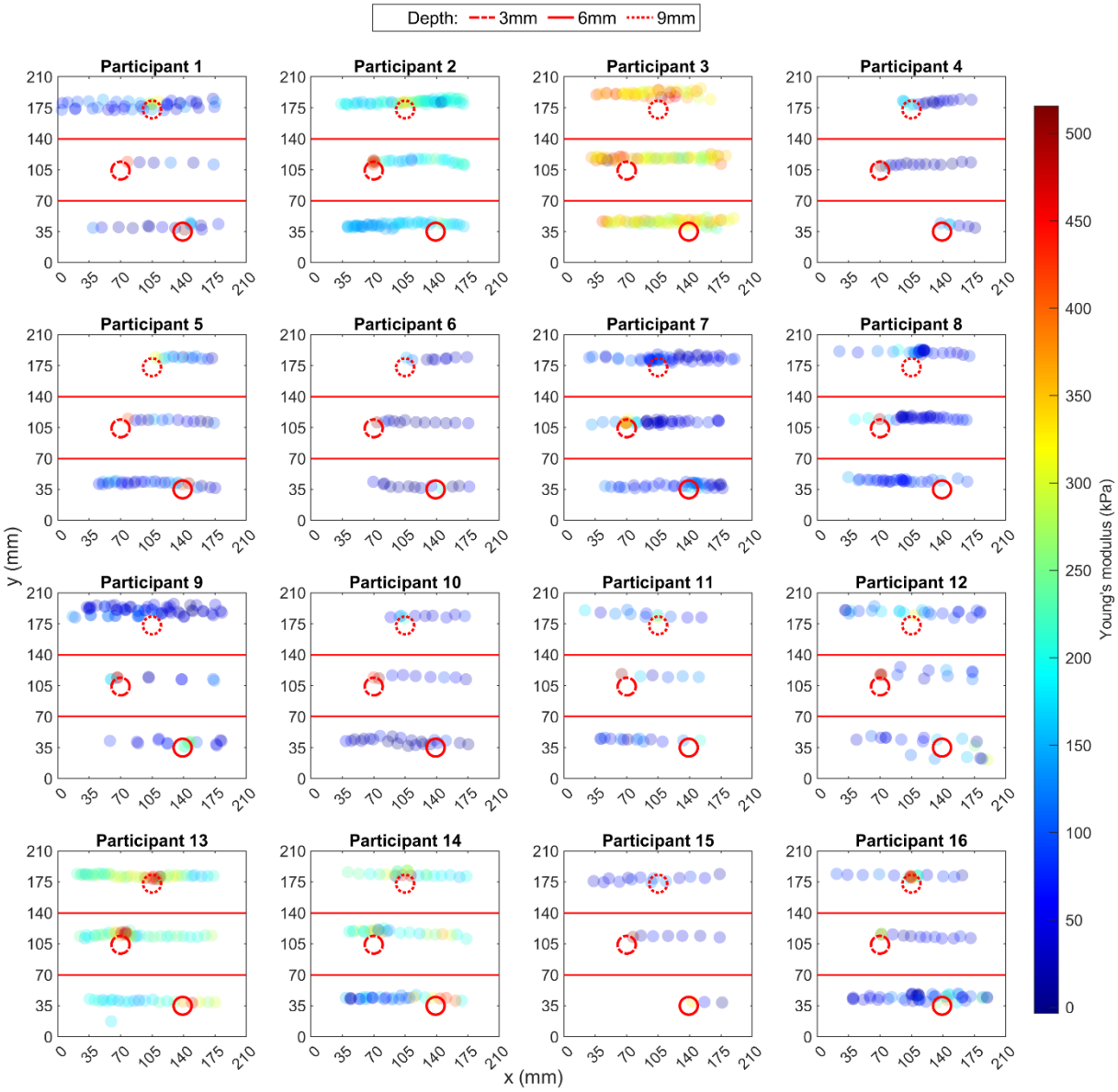

Supplementary Fig. 8 The stiffness map generated for each trial is shown here. Each point represents a palpation and its position on the phantom. The color of the point represents the measured Young's modulus (scale on the right). The position of the nodules are shown with the large, red circles.

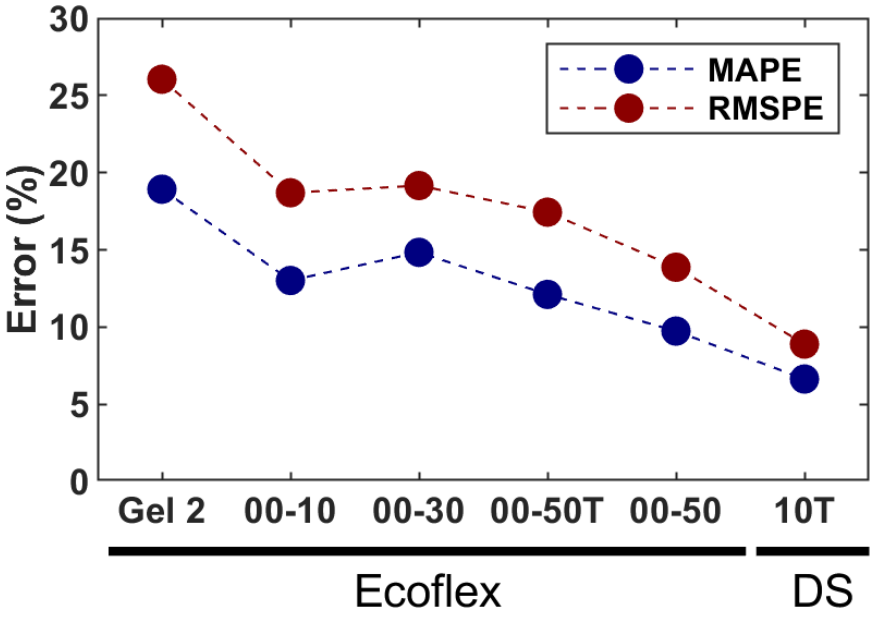

Supplementary Fig. 9 This figure shows the MAPE (blue) and RMSPE (red) between the Young's modulus values measured with SensoPal and Instron 68-TM.

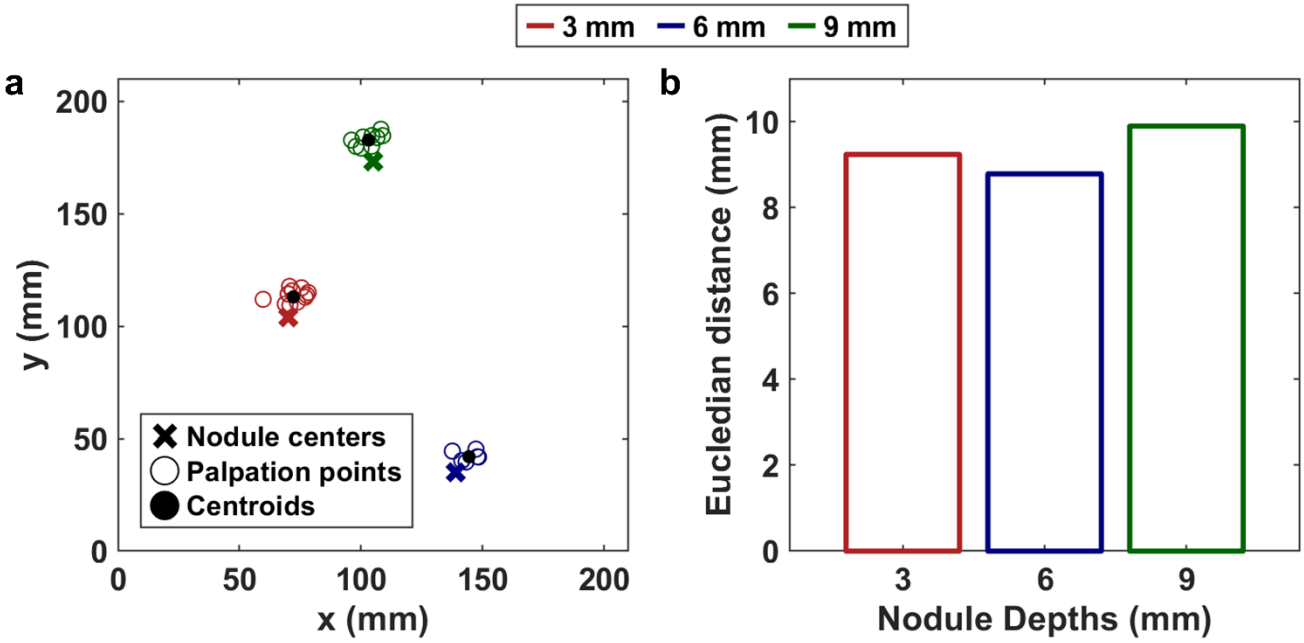

Supplementary Fig. 10 a) The positions of the final palpation points which had a Euclidean distance less than 15 mm from the nodule centers are shown here. The color of the points corresponds with the nodule depth of the trial. The crosses correspond to the position of the nodule centers. The black dots are the weighted centroids determined with equation 19. b) The Euclidean distances between the weighted centroids and the nodule centers are shown here.

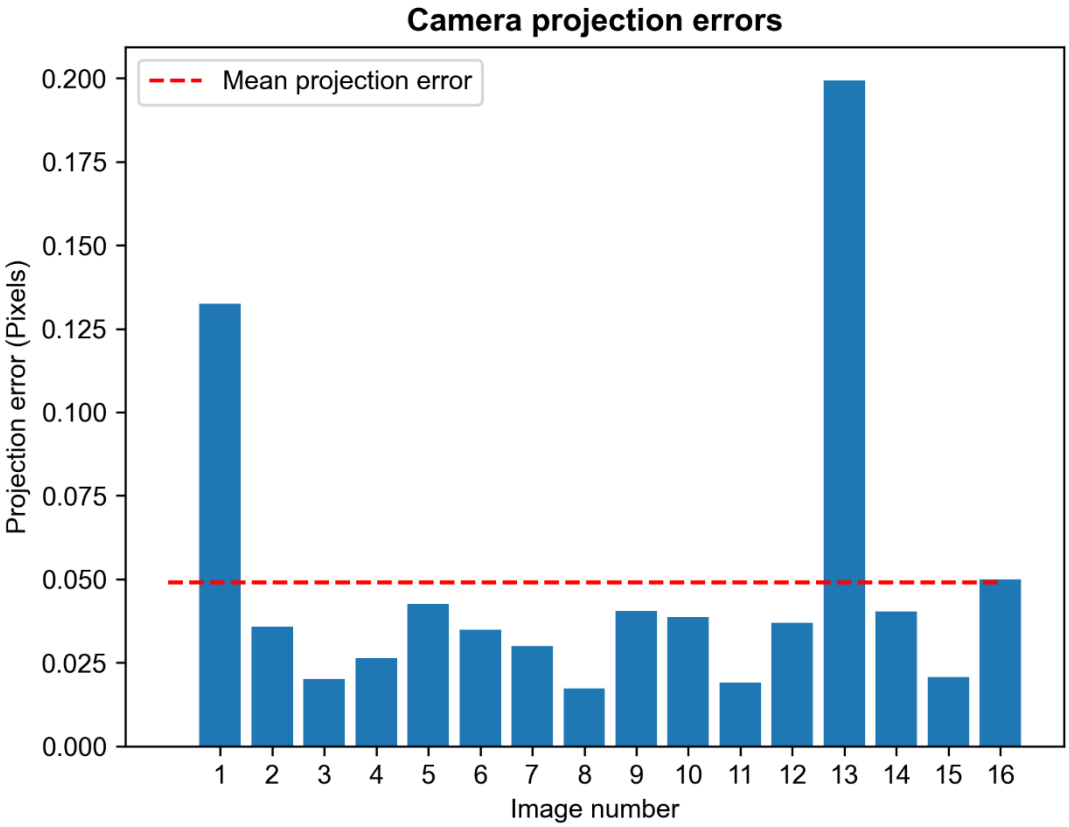

Supplementary Fig. 11 The projection error of each image where the chessboard was detected is shown here. The mean projection error is 0.0491 pixels (represented by the red line).

Prior work	Stiffness map	Palpation depth	Accuracy	Repeatability
Our work	**Yes**	**Adjustable (15mm)**	**~87% ±4%**	**~86% ±4%**
LOCK [11]	No	Fixed (1.1mm max)	~80%	N.A.
Hand-held indentation system [12]	No	Unconstrained	R^2= 0.99	94.1%
Upper abdominal palpation system [13]	No	Unconstrained	N.A.	N.A.
Piezoelectric fingers towards in-vivo breast tumor detection [14]	Yes	Tested up to 6mm	~94%	N.A.

Supplementary Table 1. Comparison between our system and existing literature. The comparison is done with a variety of existing Young's modulus measurement devices used for medical examinations.

References

[1] Fischer-Cripps, A.C., 1999. The Hertzian contact surface. *Journal of materials science*, *34*(1), pp.129-137.

[2] Lin, D.C., Shreiber, D.I., Dimitriadis, E.K. and Horkay, F., 2009. Spherical indentation of soft matter beyond the Hertzian regime: numerical and experimental validation of hyperelastic models. *Biomechanics and modeling in mechanobiology*, *8*(5), pp.345-358.

[3] Chatzipirpiridis, G., Erne, P., Ergeneman, O., Pané, S. and Nelson, B.J., 2015, August. A magnetic force sensor on a catheter tip for minimally invasive surgery. In *2015 37th Annual International Conference of the IEEE Engineering in Medicine and Biology Society (EMBC)* (pp. 7970-7973). IEEE.

[4] Madejski, G., Zbytniewski, S., Kurowski, M., Gradolewski, D., Kaoka, W. and Kulesza, W.J., 2024. Lens Distortion Measurement and Correction for Stereovision Multi-Camera System. *Engineering Proceedings*, *82*(1), p.85.

[5] Wang, J., Shi, F., Zhang, J. and Liu, Y., 2006, October. A new calibration model and method of camera lens distortion. In *2006 IEEE/RSJ International Conference on Intelligent Robots and Systems* (pp. 5713-5718). IEEE.

[6] Wei, S., He, Z. and Xie, W., 2016. Relative pose estimation algorithm with gyroscope sensor. *Journal of Sensors*, *2016*(1), p.8923587.

[7] Rodrigues, R., Barreto, J.P. and Nunes, U., 2010, September. Camera pose estimation using images of planar mirror reflections. In *European Conference on Computer Vision* (pp. 382-395). Berlin, Heidelberg: Springer Berlin Heidelberg.

[8] Guimarães, C.F., Gasperini, L., Marques, A.P. and Reis, R.L., 2020. The stiffness of living tissues and its implications for tissue engineering. *Nature Reviews Materials*, *5*(5), pp.351-370.

[9] Shergold, O.A., Fleck, N.A. and Radford, D., 2006. The uniaxial stress versus strain response of pig skin and silicone rubber at low and high strain rates. *International journal of impact engineering*, *32*(9), pp.1384-1402.

[10] Dawood, A.B., Chavali, V.K., Mack, T., Zhang, Z., Godaba, H., Angelmahr, M. and Althoefer, K., 2024. Abraded optical fibre-based dynamic range force sensor for tissue palpation. *Frontiers in Robotics and AI*, *11*, p.1489884.

[11] Cui, Z., Wang, W., Guo, L., Liu, Z., Cai, P., Cui, Y., Wang, T., Wang, C., Zhu, M., Zhou, Y. and Liu, W., 2022. Haptically quantifying Young's modulus of soft materials using a self-locked stretchable strain sensor. *Advanced Materials*, *34*(25), p.2104078.

[12] Lu, M.H., Yu, W., Huang, Q.H., Huang, Y.P. and Zheng, Y.P., 2009. A hand-held indentation system for the assessment of mechanical properties of soft tissues in vivo. *IEEE Transactions on Instrumentation and Measurement*, *58*(9), pp.3079-3085.
[13] Kato, T., Cheng, L.C., Ito, J. and Ikuta, K., 2011, November. Development of the measurement system of upper abdominal palpation. In *2011 International Symposium on Micro-NanoMechatronics and Human Science* (pp. 501-506). IEEE.
[14] Xu, X., Chung, Y., Brooks, A.D., Shih, W.H. and Shih, W.Y., 2016. Development of array piezoelectric fingers towards in vivo breast tumor detection. *Review of Scientific Instruments*, *87*(12).